J. Eur. Opt. Society-Rapid Publ. 2025, **21**, 16

https://doi.org/10.1051/jeos/2025011
Available online at: https://jeos.edpsciences.org

Journal of the European Optical Society-Rapid Publications

EOSAM 2024
Guest editors: Luca De Stefano and Raffaele Velotta

RESEARCH ARTICLE

OPEN ACCESS

Microsphere-assistance in conventional, interference and confocal microscopy – modeling and experimental results

Lucie Hüser*, Tobias Pahl, Sebastian Hagemeier, Tim Eckhardt, Felix Rosenthal, Michael Diehl, and Peter Lehmann

Measurement Technology Group, Faculty of Electrical Engineering and Computer Science, University of Kassel, Wilhelmshöher Allee 71, 34121 Kassel, Germany

Received 5 December 2024 / Accepted 5 March 2025

Abstract. Topographical as well as microscopic imaging of nanoscale surfaces plays a pivotal role across various disciplines. Nevertheless, achieving fast, label-free, and accurate characterization of laterally expanded structures below the diffraction limit remains challenging. Recent studies highlight the use of microsphere assistance for resolution improvement. Confocal, conventional, and interference microscopy, augmented by microspheres, enable the imaging of small structures that were previously inaccessible. In this contribution, results of microsphere-assisted confocal and conventional bright-field microscopy (MAM) are compared to underline the decisive role of the confocal effect. Furthermore, an extensive comparison of simulated confocal results is presented to highlight the experimental results.

Keywords: Resolution, Microsphere, Confocal microscopy, Simulation, Microsphere-assisted microscopy.

1 Introduction

In the characterization process of nanostructured surfaces, topographical measurements play a crucial role throughout different disciplines from quality control in fabrication processes to biological tissue observation. In order to further analyze surface features, the characterization process must be accurate, fast and, ideally, label-free. In microscopic and interferometric measurements, however, the system is fundamentally diffraction-limited in its lateral resolution capabilities.

With the help of microspheres, the lateral resolution of an imaging system can be extended so that surface measurements are even possible below the system's diffraction limit [1, 2]. This is demonstrated in detail for both, microscopic and interferometric applications [3–11]. The theoretical background has also been highlighted in recent studies [12–16], including a complete simulation model that incorporates a rigorous simulation of the crucial near-field wave propagation involving the microsphere [17]. Furthermore, advances have been made in mounting and application techniques of microspheres [18–21].

Confocal microscopy is a powerful tool that enhances the resolution capabilities of a conventional microscope significantly [22]. The additional confocal influence when imaging with microsphere assistance is discussed in [23–25] and also shown in [26]. Utilizing the unique optical properties of microspheres in combination with confocal microscopy for topographic measurements further increases resolving power while allowing fast processing and easy sample preparation. Measurement results show how the use of microspheres enables imaging topographical structures otherwise not accessible.

Further, we demonstrated that conventional, confocal and interference microscopes can be simply modeled based on the same theory with only slight adaptations to the respective measurement technique [27]. Based on these studies, we briefly introduce how to simulate microcylinder-assisted microscopy with focus on surface topography measurement.

Finally, studies obtained by using an finite element method (FEM) model are shown underlining the demonstrated resolution capabilities of the microsphere-assisted confocal microscope.

Parts of the outcomes presented here have already been shown beforehand [28, 29] and are extended in the context of this topical issue.

2 Methodology and instrumentation

The presented measurement results are obtained using a commercial confocal microscope (Nanofocus µsurf custom). With a numerical aperture (NA) of 0.95 and a central illumination wavelength of $\lambda = 505$ nm (LUXEON Rebel, spectral half-width = 30 nm) a high-resolution topographical measurement is already possible using the confocal effect

* Corresponding author: lucie.hueser@uni-kassel.de

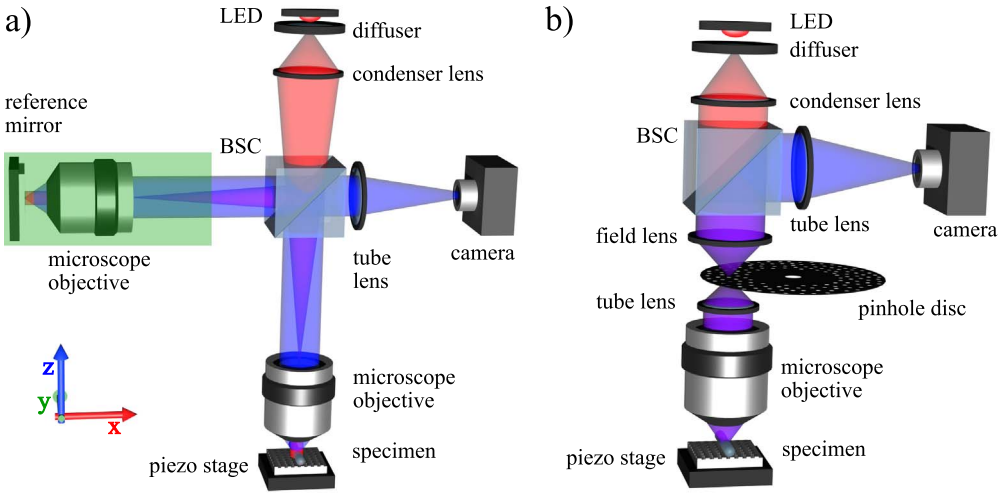

Fig. 1. Schematic representation of microcylinder-assisted conventional, interference (a) and confocal microscopes (b) showing the imaging (red) and illumination (blue) beam path. The area marked by the green rectangle corresponds to the reference arm, which is apparent in case of an interference microscope and replaced by an absorber for conventional microscopy. Note that in the measurements a microsphere is used, in the simulation this is represented by a microcylinder (BSC: beam splitter cube).

provided by an integrated pinhole disc. The measurement capabilities are described by an extensive characterization in [30].

Besides the optical limitations, the system is also limited by the pixel pitch of 7.4 µm leading to a lateral sampling interval on the specimen of $\Delta x = 163.4$ nm. Using Nyquist's sampling theorem this leads to a limited resolvable period length of $\Lambda_{\mathrm{Ny}} = 326.8$ nm. As it is shown in [30], in practice the lateral resolution of the confocal microscope corresponds to $\Lambda_{\mathrm{min}} = 0.565\ \lambda/\mathrm{NA}$ leading to $\Lambda_{\mathrm{min}} \approx 300$ nm. This results from the principle of Rayleigh's resolution criterion applied to the narrowed Point Spread Functions (PSF). The pinhole disc provides filtering in the imaging and illumination beam paths, which directly influences the image formation [31] and therefore the PSF. Following this, the significance of the results regarding high-resolution measurements should be addressed, as only a few data points per period are available. In [32] the capabilities of this system are compared with simulations taking into account the limited sampling rate. Although the results should therefore be evaluated with caution, the optical resolution capabilities of the system can be estimated.

Figure 1 shows the schematic setup including a microcylinder placed in the near-field of the specimen, a linewidth/pitch standard manufactured by supracon, which is analyzed elsewhere [33]. Taking advantage of the microsphere-induced additional magnification, the overall resolution of the optical system can be enhanced, which is shown in Section 4.

3 Model

Since all of the required modeling aspects are documented in detail, but spread over several previous publications, we compile the relevant literature and just give a short introduction. Figure 1 sketches the considered measurement setups, where conventional and interference microscopes differ in the reference arm marked by the green rectangle in Figure 1a. It should be noted that we focus on microcylinders due to significantly less computational requirements compared to microspheres.

The interaction between light and the sample with microcylinder placed on is simulated using an FEM model generally described in [34], where no microcylinder is considered. The extension to a scattering geometry including microcylinder is shown elsewhere [17]. In [27] we explain how to model all of the three considered microscope setups using the same theory approximating the light surface interaction by Kirchhoff's diffraction theory. Here, we use exactly the same instrument modeling, simply exchanging the scattered field computation by FEM.

In summary, the model can be described by the following steps:

- Rigorous 2D FEM simulations of the near field. The simulation is repeated for plane waves of different angles of the incidence, forming a conical illumination. In this way, the illumination portion of the simulation, which is the same for CSI and conventional microscopy, is represented. This method of including all possible angles of incidence within the NA of the system is chosen to represent Köhler illumination. For confocal microscopy, the illumination through the pinhole disc is represented by a delta function which is laterally shifted to various positions x_0, y_0.
- In a second step, the calculated fields are used for a far-field expansion. Fourier optics modeling is used for the mapping from object to image plane, which is calculated for each plane wave simulation separately. For confocal microscopy, the introduction of the pinhole disc as a delta-function leads to a phase shift in the Fourier plane eliminating the phase term in the Fourier series for $\mathbf{E_s}$ completely [27], assuming detection at the same pinhole as illumination.
- Depending on the setup, this is followed up by

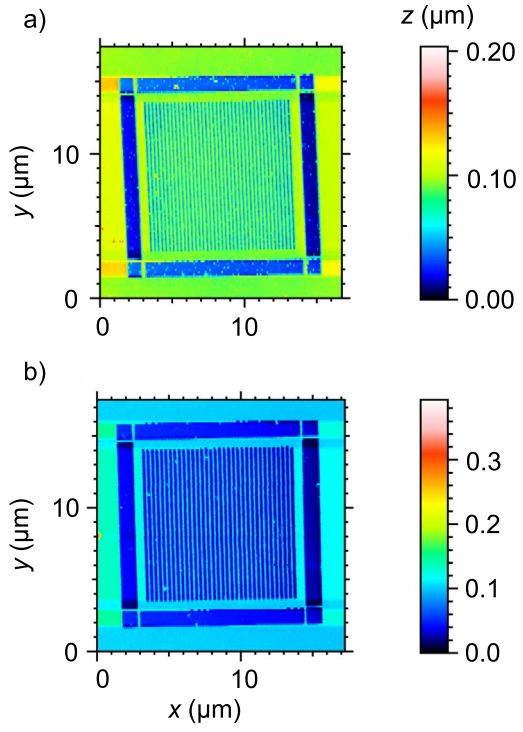

Fig. 2. Tactile AFM measurements of the a) 260 nm and b) 300 nm grating structure on the linewidth/pitch standard (fabricated by supracon [35]) for reference.

– CSI: Incoherent summation of the resulting intensity distributions, considering the reference plane field distribution. The electromagnetic field distribution considering the scattered field $\mathbf{E}_\mathrm{s}$ and the reference field $\mathbf{E}_\mathrm{ref}$ is given by

$$\mathbf{E}(x,\, z,\, \theta_\mathrm{in},\, \varphi_\mathrm{in}) = \mathbf{E_s}(x,\, z,\, \theta_\mathrm{in},\, \varphi_\mathrm{in}) + \mathbf{E}_\mathrm{ref}(x,\, \theta_\mathrm{in},\, \varphi_\mathrm{in}), \quad (1)$$

from which the intensity for each near-field computation is calculated. Therefore, the resulting intensity distribution for the complete depth scan can be described by

$$I(x,\, z) = \int_0^{2\pi} \mathrm{d}\varphi_\mathrm{in} \int_0^{\theta_\mathrm{in,max}} \mathrm{d}\theta_\mathrm{in} P^2(\theta_\mathrm{in}) I_{\theta_\mathrm{in},\varphi_\mathrm{in}}(x,z) \sin(\theta_\mathrm{in}) \cos(\theta_\mathrm{in}), \quad (2)$$

with φ_in as the incident angle and $\theta_\mathrm{in,max} = \arcsin(\mathrm{NA})$ as the maximum opening angle of the microscope objective, $P(\theta_\mathrm{in})$ representing the pupil function and $I_{\theta_\mathrm{in},\varphi_\mathrm{in}}$ as the intensity distribution for each incident angle.
– Confocal microscope: In contrast to CSI, the superposition for each incident angle is done coherently with the electromagnetic field distribution. The intensity of the resulting field is then calculated, resulting in the desired output for the depth scan.
– Conventional microscope: The electromagnetic field described in equation (1) is given by $\mathbf{E} = \mathbf{E}_\mathrm{s}$ neglecting the reference field, which is not considered for conventional microscopy. With this, the intensity distribution can be calculated likewise it is shown in equation (2).

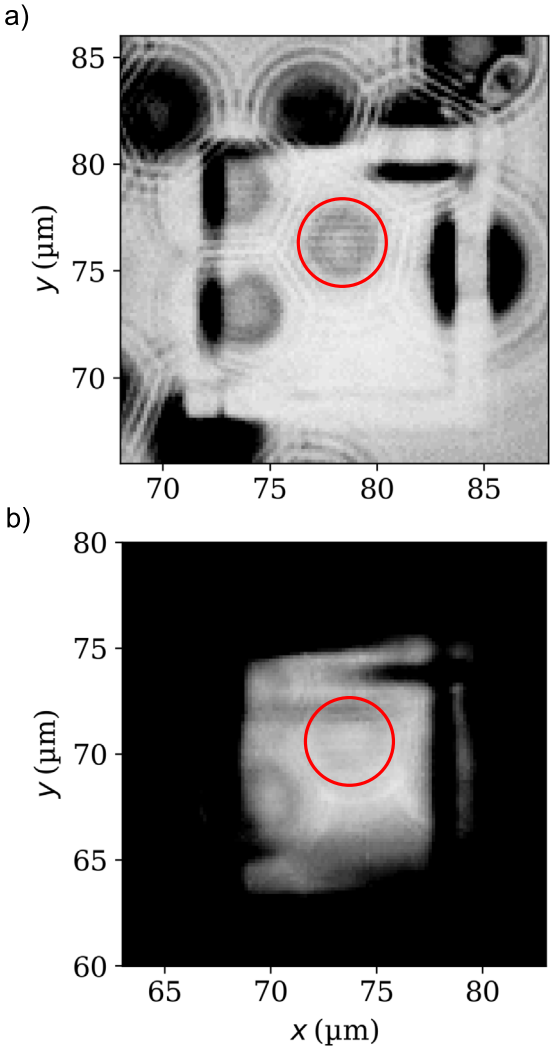

Fig. 3. Slice of an image stack acquired with confocal microscopy (a) compared to a conventional microscopic image (b) of the same field of view. The area used for the surface reconstruction shown in Figure 4 is marked in red. The complete image section shows one of the squarely arranged structures on the measurement object (supracon linewidth/pitch standard, $\Lambda_2 = 300$ nm) with the microspheres placed on it. The focal plane is selected so that the focus is visible through the microspheres. (Note that in (b) the colorbar of the image is heavily adapted to make the red-marked area sufficiently visible).

Summarizing, the different setups are all described under the same conditions and the resulting intensity distributions can be used for further analysis and comparison.

4 Measurement results

The results of the experimental investigations are presented below, with the focus on the comparison between conventional and confocal microscopy. The linewidth/pitch standard produced by supracon AG [35] is used as a sample. It offers a selection of grating structures with period lengths from 160 nm to 4 µm. Since the presented results only show

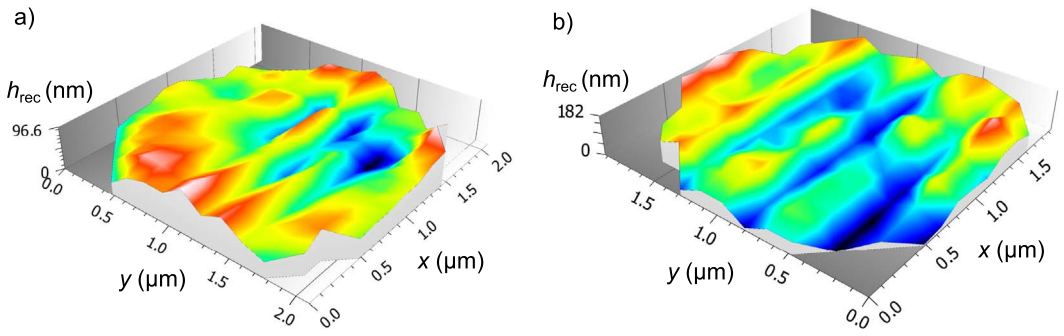

Fig. 4. Confocal microsphere-assisted topography measurements of grating structures on the linewidth/pitch standard. Reconstructed surface data is shown for a period length of a) $\Lambda_1 = 260$ nm and b) $\Lambda_2 = 300$ nm. The limited field of view induced by the microspheres (SiO_2, diameter $d = 5$ µm) is visible as a circular cut-out of the measurement area. The additional magnification introduced by the microsphere leads to enlarged period lengths in the measurement results.

a small field of view, Atomic Force Microscope (AFM) measurements of the structures used are included to provide a better overview on the specimen. The results are shown in Figure 2. In particular, the structures with $\Lambda_1 = 260$ nm (height: 55 nm) and $\Lambda_2 = 300$ nm (height: 85 nm) are important for the following experiments, as they are close to the optical resolution limit of the confocal microscope. The microspheres are made of SiO_2 and have a diameter of 5 µm (fabricated by micromod Partikeltechnologie GmbH).

An image stack is recorded with a confocal microscope. Depth scanning in the z-direction provides the signals required for further signal processing. In the focal plane, the result is compared with an image of the same field of view taken with conventional microscopy. When comparing the confocal microsphere-assisted result with the MAM image of the same field of view in Figure 3, it becomes clear that the confocal technique affects the imaging process. The image of the conventional microscope provides significantly lower contrast in the region of interest, as it is shown in Figure 3b. It does not sufficiently resolve the $\Lambda_2 = 300$ nm structure, whereas in Figure 3a, the contrast is improved due to the confocal effect which is beneficial for microsphere-assisted imaging. As introduced in Figure 2, the square surrounding of the grating structure also becomes visible.

After acquiring the image stack, topography data are reconstructed by appropriate signal analysis algorithms. 3D representations of measured surfaces for different grating periods ($\Lambda_1 = 260$ nm and $\Lambda_2 = 300$ nm) are shown in Figure 4. Neither structure is resolvable with conventional or confocal microscopy without microsphere-assistance due to the large pixel pitch of the camera. Additionally, the period length of 260 nm is below the optical resolution limit of the system. The additional magnification induced by the microspheres is $M \approx 1.3$. The limited camera resolution of the commercially available confocal microscope becomes relevant when measuring small structures. Nevertheless, the resolution of the system is improved overall by the use of microspheres, as the topographic measurement of $\Lambda_1 = 260$ nm shows. In order to clarify about the optical resolution enhancement by the microsphere, a comparison with the simulated data is shown in the subsequent chapter.

5 Simulation

For comparison, simulations are carried out with the previously presented model. A microcylinder with radius $r = 2.5$ µm and refractive index $n = 1.4621$ [36] is placed on a structure similar to the linewidth/pitch standard used in the measurements. It contains a SiO_2 substrate with a silicon structure ($n_{Si} = 4.2620 + 0.045187i$, [37]) on top forming gratings of period lengths $\Lambda_1 = 260$ nm (step height $h_{0,1} = 55$ nm) and $\Lambda_2 = 300$ nm (step height $h_{0,2} = 85$ nm). The arrangement of microcylinder and grating is assumed to have periodic boundary conditions with a period length of 13.2 µm. A microcylinder instead of a microsphere is used in order to achieve reasonable computation times. The illuminating light of wavelength $\lambda = 505$ nm is considered to be monochromatic and TM polarized and the numerical aperture (NA) of the microscope objective lens is 0.95. Figure 5 shows cross-sections of image stacks obtained for conventional (Figs. 5a and 5b), interference (Figs. 5c and 5d), and confocal (Figs. 5e and 5f) microscopy for both period lengths. Note that more information on definition of the polarization are provided in a previous publication [34]. In agreement with previous observations [12, 38], the influence of the grating appears more pronounced for TM polarization in the area of the cylinder and therefore only the results for TM polarization are shown. Especially for interference and confocal microscopy, the grating can be recognized in the phase (interference) and contrast (confocal) of the image stacks (the areas of interest are marked in green). It should be noted that the grating considered as a measurement object more or less corresponds to a phase grating and hence only a weak influence on conventional microscope images is to be expected. For results of amplitude gratings we refer to [38]. Furthermore, the simulated image stacks shown in Figure 5 underline the observation that in the imaging process with microsphere-assistance the role of non-linearity should not be neglected when analyzing the data. Changing the period length

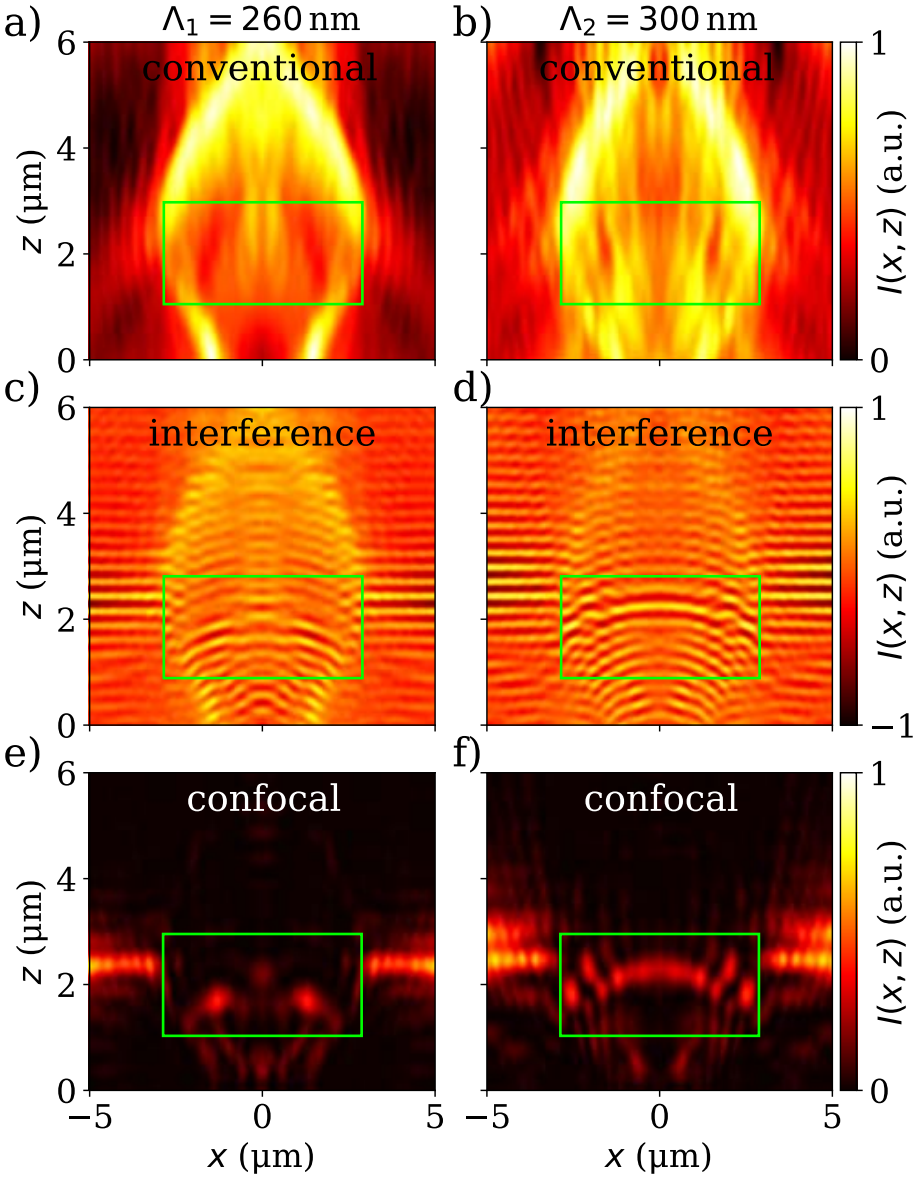

Fig. 5. Image stacks simulated for conventional (a, b), interference (offset-reduced) (c, d) and confocal (e, f) microscopy assuming either 260 nm (a, c, e) or 300 nm (b, d, f) period length of the grating. TM polarized light with $\lambda = 505$ nm is used. The microcylinder extends from $x = -2.5$ µm to $x = 2.5$ µm. The areas of interest for interference and confocal microscopy are marked in green.

leads to significant changes in the intensity distributions and the phase behavior for all three setups considered.

The analysis goes one step further by taking a closer look at confocal imaging in direct comparison with the measurement results shown in Section 4. Thus, assuming a sinusoidal structure (silicon, peak-to-peak amplitude 50 nm, $\Lambda_1 = 260$ nm and $\Lambda_2 = 300$ nm) and TM-polarized light ($\lambda = 505$ nm), rigorous simulations are performed based on the model presented in Section 3 with and without microcylinder support. Near the resolution limit, the influence of the sample on phase/contrast of the simulated image stack is marginal. In order to obtain a meaningful evaluation of the results, two simulations are therefore carried out for each case, one of them with a phase shift of 180° of the sinusoidal structure as described in [17]. The difference between the results $I(x, z)$ and $I_{\text{inv}}(x, z)$ is calculated, resulting in $\Delta I(x, z)$. Figure 6 shows the resulting intensity distributions.

Taking the difference $\Delta I(x, z)$ into account, the results can be interpreted as follows: if the information is still present in the contrast, some periodicity is visible in $\Delta I(x, z)$ and thus, the theoretical resolution capability can be obtained. If this is taken into account, it can be seen that the structure with 260 nm period length cannot be resolved by the confocal system without the microcylinder (Fig. 6b), but can be resolved with microcylinder-assistance (Fig. 6d). In contrast, for $\Lambda_2 = 300$ nm residues indicating a resolved structure can be observed in both cases (Figs. 6f and 6h).

The assumptions about the sinusoidal structure visible in the contrast, especially in the simulations with microcylinder support, are confirmed by the reconstructed

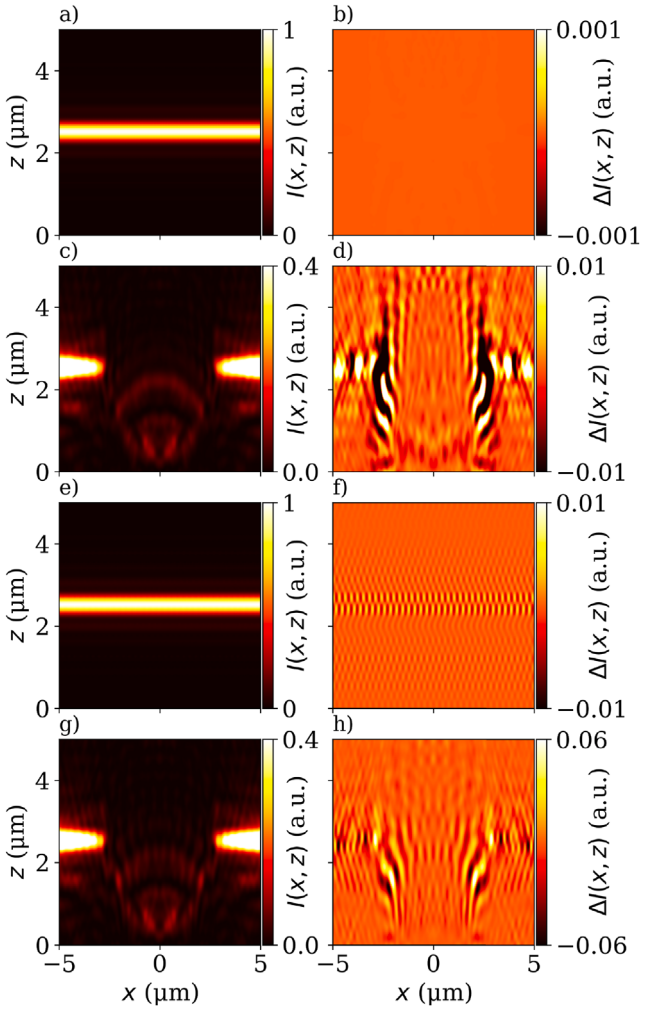

Fig. 6. Intensity distributions for simulated confocal study cases. The first column shows the $I(x, z)$ for the sinusoidal grating for $\Lambda_1 = 260$ nm (a, c) and $\Lambda_2 = 300$ nm (e, g). The second column depicts $\Delta I(x, z)$, respectively. In c), d) and g), h) the results with microcylinder-assistance are shown. (The intensity distributions for $I_{\text{inv}}(x, z)$ are not plotted).

surface $h_{\text{rec}}(x)$. Since the cylinder introduces aberrations mainly towards the edges of the field of view, the difference for both structures (phase shift 0° and 180°) is again calculated, which leads to $\Delta h_{\text{rec}}(x) = h_{\text{rec}}(x) - h_{\text{rec,inv}}(x)$. In Figure 7 this is shown for a) $\Lambda_1 = 260$ nm and b) $\Lambda_2 = 300$ nm.

Overall, the reconstruction results show something like a sinusoidal surface overlaid by strong aberrations. In Figure 7b some outliers can be recognized, which are probably due to the sensitivity of the signal processing algorithm to irregularities. These simulation results underline the experimental results shown in Figure 4.

6. Conclusion

Confocal microscopy is a powerful tool that enhances depth sectioning and the lateral resolution capabilities of a conventional microscope. When coupled with microsphere-assistance, this technique achieves even higher resolution.

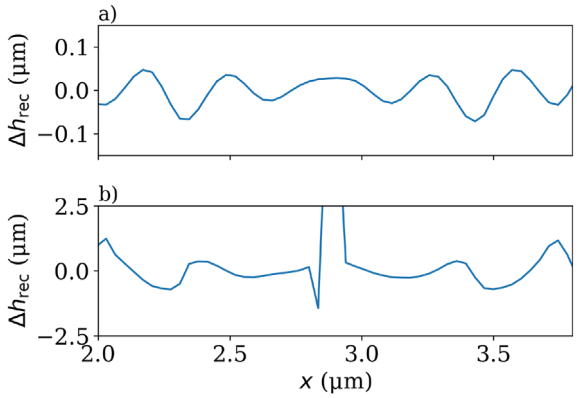

Fig. 7. Difference of reconstructed surface profiles for a) $\Lambda_1 = 260$ nm and b) $\Lambda_2 = 300$ nm with microcylinder-assistance. The difference is taken from each simulation with the reconstructed surfaces $h_{\text{rec}}(x)$ and $h_{\text{rec,inv}}(x)$.

Like it is discussed in [24], the confocal effect on microscopic imaging plays a pivotal role in the capability of the system to resolve structures below the diffraction limit. Furthermore, for commercially available systems the pixel resolution can be improved due to the additional magnification by the microspheres. Additionally, a method is introduced to simulate measurement results obtained by microcylinder-assisted conventional, interference, and confocal microscopy as the most common optical profiling techniques. With a simulation study on the difference an added microcylinder makes for confocal imaging, conclusions can be drawn on the resolution capabilities of the system. The resolution enhancement observed in the simulation validates the experimental results.

Future investigations considering rigorous simulations should meticulously analyze the transfer behavior of a confocal microscope considering microspheres, enabling a comprehensive comparison with MAM and interference microscopy. Simulations will be performed for these instruments to study resolution enhancement capabilities using e.g. approaches presented in literature [17, 38, 39] in order to elucidate the potential of MAM.

Funding

The partial support of this work by the Deutsche Forschungsgemeinschaft (DFG, LE992/15-3) is gratefully acknowledged.

Conflicts of interest

The authors have no conflicts of interest to declare.

Data availability statement

The data that support the findings of this study are available upon reasonable request from the authors.

Author contribution statement

According to the Contributor Role Taxonomy (CRediT) the authors' contributions are:

L. Hüser: Conceptualization, investigation, formal analysis, data curation, visualization, writing.

T. Pahl: Methodology, investigation, formal analysis, data curation, visualization, writing.

S. Hagemeier: Investigation.

T. Eckhardt: Investigation.
F. Rosenthal: Methodology.
M. Diehl: Resources.
P. Lehmann: Funding acquisition, conceptualization, supervision.

References

1 Wang Z, et al., Optical virtual imaging at 50 nm lateral resolution with a white-light nanoscope, *Nat. Commun.* **2**, 218 (2011). https://doi.org/10.1038/ncomms1211.
2 Darafsheh A, Microsphere-assisted microscopy, *J. Appl. Phys.* **131**, 031102 (2022). https://doi.org/10.1063/5.0068263.
3 Abbasian V, Pahl T, Hüser L, Lecler S, Montgomery P, Lehmann P, Darafsheh A, Microsphere-assisted quantitative phase microscopy: a review, *Light Adv. Manuf.* **5**, 1 (2024). https://doi.org/10.37188/lam.2024.006.
4 Darafsheh A, et al., Optical super-resolution by high-index liquid-immersed microspheres, *Appl. Phys. Lett.* **101**, 141128 (2012). https://doi.org/10.1063/1.4757600.
5 Wang F, et al. Three-dimensional super-resolution morphology by near-field assisted white-light interferometry, *Sci. Rep.* **6**, 24703 (2016). https://doi.org/10.1038/srep24703.
6 Upputuri PK, Pramanik M, Microsphere-aided optical microscopy and its applications for super-resolution imaging, *Opt. Commun.* **404**, 32 (2017). https://doi.org/10.1016/j.optcom.2017.05.049.
7 Montgomery P, et al., 3D nano surface profilometry by combining the photonic nanojet with interferometry, *J. Phys. Conf. Ser.* **794**, 012006 (2017). https://doi.org/10.1088/1742-6596/794/1/012006.
8 Montgomery P, Perrin S, Lecler S, in 20th International Conference on Transparent Optical Networks (ICTON), Bucharest, Romania, July 1–5 (2018). https://doi.org/10.1109/ICTON.2018.8473839.
9 Kassamakov I, et al., 3D super-resolution optical profiling using microsphere enhanced mirau interferometry, *Sci. Rep.* **7**, 3683 (2017). https://doi.org/10.1038/s41598-017-03830-6.
10 Wang J, et al., Microsphere-assisted dark-field microscopy based on a fully immersed low refractive index microsphere, *Opt. Lett.* **48**, 1858 (2023). https://doi.org/10.1364/OL.482922.
11 Astratov VN, et al., Roadmap on label-free super-resolution imaging, *Laser Photonics Rev.* **17**, 2200029 (2023). https://doi.org/10.1002/lpor.202200029.
12 Hüser L, Pahl T, Lehmann P, Experimental and numerical polarization analysis of the 3D transfer behavior in microsphere assisted interferometry for 1D phase gratings, *J.* Eur. Opt. Soc. Rapid Publ. **19**, 32 (2023). https://doi.org/10.1051/jeos/2023029.
13 Yang H, et al., Super-resolution imaging of a dielectric microsphere is governed by the waist of its photonic nanojet, *Nano Lett.* **16**, 4862 (2016). https://doi.org/10.1021/acs.nanolett.6b01255.
14 Perrin S, et al., Role of coherence in microsphere-assisted nanoscopy, *Proc. Modeling Aspects in Optical Metrology VI, SPIE* **10330**, 103300V (2023). https://doi.org/10.1117/12.2270246.
15 Boudoukha R, et al., Near-to far-field coupling of evanescent waves by glass microspheres, *Photonics* **8**, 73 (2021). https://doi.org/10.3390/photonics8030073.
16 Darafsheh A, Abbasian V, Dielectric microspheres enhance microscopy resolution mainly due to increasing the effective numerical aperture, *Light Sci. Appl.* **12**, 22 (2023). https://doi.org/10.1038/s41377-022-01056-4.
17 Pahl T, et al., FEM-based modeling of microsphere-enhanced interferometry, *Light Adv. Manuf.* **3**, 699 (2022). https://doi.org/10.37188/lam.2022.049.
18 Zyla G, et al., 3D micro-devices for enhancing the lateral resolution in optical microscopy , *Light Adv. Manuf.* **5**, 19 (2024). https://doi.org/10.37188/lam.2024.019.
19 Hong Y, et al., Microsphere probe: combining microsphere-assisted microscopy with AFM, *Opt. Express* **31**, 27520 (2023). https://doi.org/10.1364/OE.494572.
20 Perrin S, et al., Miniaturized microsphere-assisted microscopy, *Appl. Phys. Lett.* **122**, 161108 (2023). https://doi.org/10.1063/5.0135346.
21 Trukhova A, et al., Microlens-assisted microscopy for biology and medicine, *J. Biophotonics* **15**, e202200078 (2022). https://doi.org/10.1002/jbio.202200078.
22 Wilson T, Resolution and optical sectioning in the confocal microscope, *J. Micros.* **244**, 113 (2011). https://doi.org/10.1111/j.1365-2818.2011.03549.x.
23 Allen KW, et al., Super-resolution microscopy by movable thin-films with embedded microspheres: resolution analysis, *Ann. Phys.* **527**, 513 (2015). https://doi.org/10.1002/andp.201500194.
24 Darafsheh A, Comment on "Super-resolution microscopy by movable thin-films with embedded microspheres: resolution analysis" [Ann. Phys. (Berlin) 527, 513 (2015)], *Ann. Phys.* **528**, 898 (2016). https://doi.org/10.1002/andp.201500359.
25 Allen KW, Li Y, Astratov VN, Reply to "Comment on "Super-resolution microscopy by movable thin-films with embedded microspheres: resolution analysis" [Ann. Phys. (Berlin) 527, 513 (2015)]", *Ann. Phys.* **528**, 901 (2016). https://doi.org/10.1002/andp.201600211.
26 Yan Y, et al., Microsphere-coupled scanning laser confocal nanoscope for sub-diffraction-limited imaging at 25 nm lateral resolution in the visible spectrum, *ACS Nano* **8**, 1809 (2014). https://doi.org/10.1021/nn406201q.
27 Pahl T, et al., Electromagnetic modeling of interference, confocal, and focus variation microscope, *Adv. Photonics Nexus* **3**, 016013 (2024). https://doi.org/10.1117/1.APN.3.1.016013.
28 Hüser L, et al., Microsphere-assistance in microscopic and confocal imaging, *EPJ Web Conf.* **309**, 02014 (2024). https://doi.org/10.1051/epjconf/202430902014.
29 Pahl T, et al., Modeling microcylinder-assisted conventional, interference and confocal microscopy, *EPJ Web Conf.* **309**, 02015 (2024). https://doi.org/10.1051/epjconf/202430902015.
30 Hagemeier S, *Ph.D. thesis*, University of Kassel, 2022.
31 Goodman J, *Introduction to Fourier Optics*, 2nd edn (McGraw-Hill Book Company, New York, 1996).
32 Pahl T, et al., Rigorous 3D modeling of confocal microscopy on 2D surface topographies, *Meas. Sci. Technol.* **32**, 094010 (2021). https://doi.org/10.1088/1361-6501/abfd69.
33 Hüser L, Lehmann P, Microsphere-assisted interferometry with high numerical apertures for 3D topography measurements, *Appl. Opt.* **59**, 1695 (2020). https://doi.org/10.1364/AO.379222.
34 Pahl T, et al., 3D modeling of coherence scanning interferometry on 2D surfaces using FEM, *Opt. Express* **28**, 39807 (2020). https://doi.org/10.1364/OE.411167.
35 Huebner U, et al., A nanoscale linewidth/pitch standard for high-resolution optical microscopy and other microscopic

techniques, *Meas. Sci. Technol.* **18**, 422 (2007). https://doi.org/10.1088/0957-0233/18/2/S14.
36 Malitson IH, Interspecimen comparison of the refractive index of fused silica, *J. Opt. Soc. Am.* **55**, 1205 (1965). https://doi.org/10.1364/JOSA.55.001205.
37 Schinke C, et al., Uncertainty analysis for the coefficient of band-to-band absorption of crystalline silicon, *AIP Adv.* **5**, 67168 (2015). https://doi.org/10.1063/1.4923379.
38 Pahl T, et al., Simulative investigation of microcylinder-assisted microscopy in reflection and transmission mode, Proc, *Modeling Aspects in Optical Metrology IX, SPIE* **12619**, 12619OK (2023). https://doi.org/10.1117/12.2673443.
39 Maslov AV, Astratov VN, Origin of the super-resolution of microsphere-assisted imaging, *Appl. Phys. Lett.* **124**, 061105 (2024). https://doi.org/10.1063/5.0188450.